frontiers in Energy Research

ORIGINAL RESEARCH
published: 26 March 2021
doi: 10.3389/fenrg.2021.657962

Studies of $Li_2Fe_{0.9}M_{0.1}SO$ Antiperovskite Materials for Lithium–Ion Batteries: The Role of Partial Fe^{2+} to M^{2+} Substitution

Mikhail V. Gorbunov[1], Salvatore Carocci[1], Ignacio G. Gonzalez Martinez[1], Volodymyr Baran[2] and Daria Mikhailova[1]**

[1] Leibniz Institute for Solid State and Materials Research (IFW) Dresden e.V., Dresden, Germany, [2] Deutsches Elektronen-Synchrotron (DESY), Hamburg, Germany

OPEN ACCESS

Edited by:
Ismael Saadoune,
Cadi Ayyad University, Morocco

Reviewed by:
Prabeer Barpanda,
Indian Institute of Science (IISc), India
Ting-Feng Yi,
Northeastern University at Qinhuangdao, China
Ghulam Ali,
National University of Sciences and Technology (NUST), Pakistan

***Correspondence:**
Mikhail V. Gorbunov
m.gorbunov@ifw-dresden.de
Daria Mikhailova
d.mikhailova@ifw-dresden.de

Specialty section:
This article was submitted to Electrochemical Energy Conversion and Storage, a section of the journal Frontiers in Energy Research

Received: 24 January 2021
Accepted: 08 March 2021
Published: 26 March 2021

Citation:
Gorbunov MV, Carocci S, Gonzalez Martinez IG, Baran V and Mikhailova D (2021) Studies of $Li_2Fe_{0.9}M_{0.1}SO$ Antiperovskite Materials for Lithium–Ion Batteries: The Role of Partial Fe^{2+} to M^{2+} Substitution. Front. Energy Res. 9:657962. doi: 10.3389/fenrg.2021.657962

Cubic $Li_2Fe_{0.9}M_{0.1}SO$ antiperovskites with M–Co^{2+}, or Mn^{2+} were successfully synthesized by a solid-state technique, and studied as cathode materials in Li-batteries. The influence of the Co, and Mn cation substitution of Fe in Li_2FeSO on the resulting electrochemical performance was evaluated by galvanostatic cycling, while the reaction mechanism was explored by applying *operando* X-ray absorption and X-ray diffraction techniques using synchrotron radiation facilities. Even 10% Fe-substitution by these metals completely changes the structural behavior of the material upon Li-removal and insertion, in comparison to Li_2FeSO. The Co-substitution significantly improves cyclability of the material at high current densities in comparison to the non-substituted material, reaching a specific capacity of 250 mAh/g at 1C current density. In contrast, the Mn-substitution leads to deterioration of the electrochemical performance because of the impeded kinetics, which may be caused by the appearance of a second isostructural phase due to formation of Jahn-Teller Mn^{3+} cations upon delithiation.

Keywords: chemical flexibility, redox activity, non-linear structure change, cathode materials, high specific capacity

INTRODUCTION

Even though currently existing Li-ion battery materials are satisfying most of the consumers requirements, there is always space for improvement, particularly in the field of cathode materials as they primarily determine the price and the electrochemical performance of the battery. Search for novel materials that would be cheaper, safer and would demonstrate better characteristics is actual as long as the technological development in the market of portable electronics or electric vehicles exists, which is mostly dominated by LIB as the energy sources (Wu et al., 2020).

Recently reported compounds with the antiperovskite structure represent an interesting class of materials for possible application as cathodes in Li-ion batteries (Lai et al., 2017, 2018; Mikhailova et al., 2018; Gorbunov et al., 2020). Among the studied materials, Li_2CoSO and Li_2MnSO (Lai et al., 2018), Li_2FeSO (Lai et al., 2017; Mikhailova et al., 2018) and $Li_2Fe_{0.5}Mn_{0.5}SO$ (Gorbunov et al., 2020), the Li_2FeSO compound demonstrates the most promising characteristics in terms of

specific electrochemical capacities during galvanostatic cycling and rate capability. Other materials mentioned above show much lower specific capacity values not exceeding 100 mAh/g after few cycles (Lai et al., 2018) and quite a poor cycling behavior in lithium cells (Gorbunov et al., 2020). The structure of antiperovskites differs significantly from known tunnel-like (olivine) (Padhi et al., 1997), two-dimensional (α-$NaFeO_2$) (Demourgues Guerlou et al., 1993), three-dimensional (spinel $LiMn_2O_4$) (Thackeray et al., 1983), or polyanionic NASICON- or LISICON-type structures (Bukun et al., 1998), commonly used as cathodes for Li-ion or Na-ion batteries.

In the *Pm-3m* antiperovskite structure, cations and anions have inverse atomic sites as compared to the classic perovskite $CaTiO_3$ phase. S^{2-} anions occupy the corners of a cubic primitive cell, while O^{2-} occupies its center and metal cations the center of each face, sharing the site.

The main advantage of cubic Li_2MSO antiperovskite materials in comparison to commonly used cathodes is an outstanding value of theoretical specific capacity: up to 1.25 Li may be extracted from the unit cell before the structure collapses, according to theoretical calculations (Lu and Ciucci, 2018), giving a capacity value of more than 270 mAh/g, in dependence on the composition of the material. However, there are some drawbacks like relatively low operation voltage, which nevertheless may possibly be overcome by investigating the chemical flexibility of the antiperovskites.

The goal of the current research was to study the influence of the partial substitution of Fe by other redox-active transition metal cations on the resulting structural and electrochemical properties of Li_2FeSO. It was shown that due to the high chemical flexibility of antiperovskite materials, even minor cation substitution can dramatically change structure evolution during Li-removal and improve electrochemical performance toward cycling stability at high current densities.

MATERIALS AND METHODS

Synthesis and PXRD Analysis

The compositions $Li_2Fe_{0.9}Co_{0.1}SO$, $Li_2Fe_{0.9}Mn_{0.1}SO$ and the Li_2FeSO reference material were synthesized by a solid-state reaction between stoichiometric amounts of Li_2O (Alfa Aesar, 99.5%), elemental sulfur (Sigma Aldrich, $\geq$99.9%) and transition metals Co, Fe, and Mn (all of them from Alfa Aesar, >99.9%). The mixture of reagents (total mass around 0.5 g) was thoroughly grinded in an agate mortar, pressed into a pellet and put into a corundum crucible, which was placed into a quartz tube. All of the described manipulations were done in an Ar-filled glovebox to avoid water adsorption on the surface of initial reagents. The quartz tube was subsequently evacuated to 10^{-5} mBar and then filled with argon to 0.5 Bar before melt-sealing it. The volume of the ampule was around 20 cm^3. Afterward, the ampule with the pellet was put in an oven, heated up to 750°C with a rate of 50°C/h, kept there for 3 h, and immediately cooled down to room temperature by quenching it in melting ice. In general, the synthesis route was taken from the previous reports on antiperovskites (Lai et al., 2018; Gorbunov et al., 2020); however, some parameters were varied to optimize the quality of the obtained materials.

To check the phase purity of the materials and to calculate the crystallographic unit cell parameters, powder X-ray diffraction studies were done on laboratory X-ray diffractometer STOE Stadi P, with $MoK_{\alpha 1}$ radiation and Ge (111) monochromator in Debye-Scherrer geometry. All preparations for the measurements were done in an Ar-filled glovebox to avoid decomposition of the materials in air. JANA 2006 program (Petricek et al., 2014) was used in order to perform structural analysis of the obtained X-ray diffractograms using Rietveld refinement (Rietveld, 1969).

Transmission Electron Microscopy

Transmission Electron Microscopy (TEM) studies were conducted on a FEI Titan 300–80 TEM with third-order spherical aberration correction. The $Li_2Fe_{0.9}Mn_{0.1}SO$ and $Li_2Fe_{0.9}Co_{0.1}SO$ powders were loaded by direct contact onto Cu 300 mesh TEM grids (Agar) and holey carbon film on Cu 300 mesh TEM grids (Plano). High-resolution imaging was done at 300 kV.

Electrochemical Studies

All electrochemical tests were performed on a multichannel potentiostat VMP3 (BioLogic) at room temperature in two- or three-electrode Swagelok cells. The electrolyte consisted of 1 M lithium bis(trifluoromethanesulfonyl)imide, LiTFSI (99.95%, Sigma-Aldrich), dissolved in a mixture of DME (dymethoxyethane, Sigma Aldrich, 99.5%) and DOL (1,3-dioxolane, Sigma Aldrich, 99.8%) 1:1 by volume. Metallic lithium (Alfa Aesar, 99.8%) served as a counter electrode, and in case of the three-electrode setup, also as a reference electrode. The working electrode represented a mixture of the antiperovskite material, carbon black or carbon nanotubes as a conductive additive, and Polytetrafluoroethylene (PTFE, Sigma Aldrich) binder in 80:10:10% mass ratio, respectively, which was pressed on a steel or aluminum mesh.

Galvanostatic cycling with potential limitation was carried out in the two-electrode set-up in order to estimate the rate capabilities of the materials and their stability during long-term cycling. Various current densities were applied throughout 50 cycles. The value of 1C corresponds to the extraction (insertion) of 1 Li^+ ion from(into) the $Li_2Fe_{0.9}M_{0.1}SO$ formula unit within an hour. Long-term cycling was performed at a 1C current density. A mass loading was around 5 mg/cm^2.

A low scan rate cyclic voltammetry technique was applied in the two-electrode set-up to preliminarily estimate redox processes during extraction and insertion of Li^+ ions. The voltage sweeping rate was 0.05 mV/s.

Galvanostatic intermittent titration measurements were done for kinetical characterization of lithium extraction/insertion from/into the $Li_2Fe_{0.9}M_{0.1}SO$ structure in a three-electrode set-up. The duration of the current pulse with 0.1C was 10 min, and the relaxation time was 8 h. The experimental parameters for calculations were as following: the surface area of the electrode material with the mass of about 3.28 mg was 1.130 cm^2, the crystallographic density and the volume of the material were 3.281 g/cm^3, and 10^{-3} cm^3, respectively. The values of lithium

diffusion coefficients at different potentials were calculated according to work (Weppner and Huggins, 1977).

Operando Synchrotron Studies

In order to characterize changes in the electronic and local structure of the materials during Li-removal and insertion, *operando* X-ray absorption spectroscopy studies were performed on the P65 beamline of DESY (Hamburg, Germany) (Welter et al., 2018). The experiments were carried out using coin cells with Kapton windows, which were put into an eightfold coin cell holder (Herklotz et al., 2016), connected to a multichannel potentiostat VMP3 (Biologic), similar to laboratory electrochemical experiments. K-edge spectra of Fe, Mn, and Co were recorded every hour while the cells were charged and discharged at 0.1C current density. Appropriate metallic foils were used for energy calibration, while transition metal oxides or salts were used as reference materials for metal oxidation states. The electrolyte used was LP30, consisting of 1M $LiPF_6$ in the mixture of ethylene carbonate and dimethyl carbonate (1:1 by volume, BASF). Software packet Demeter (Ravel and Newville, 2005) was used to analyze the obtained data. The spectra were recorded in transmission and fluorescence yield mode.

Operando X-ray diffraction experiments were performed on the BL04–MSPD beamline at ALBA (Barcelona, Spain) (Fauth et al., 2013) and on the P02.1 beamline at DESY (Hamburg, Germany) (Dippel et al., 2015). The measurements were carried out using coin cells with quartz windows and the same eightfold holder. Each diffraction pattern was recorded every 10 min, while the cells were charged and discharged at 0.1C current density. The electrolyte was the same as for *operando* XAS measurements.

RESULTS

Synthesis and Primary Physicochemical Characterization

The main challenge of the Li_2MSO synthesis in a closed ampule relates to the high volatility of sulfur at high temperatures and, as a consequence, its removal from the reaction zone and changes in the stoichiometry of the solids. The presence of some amount of sulfur in the gas phase during the reaction time was often confirmed after the synthesis by an off-white scurf-like layer on the wall of the ampule and therefore, a slight amount of impurities was likely to form. When the initial argon pressure inside the tube was increased in comparison to the earlier reported synthetic conditions for $Li_2Fe_{1-x}M_xSO$ series (Gorbunov et al., 2020), the scurf disappeared, in accordance with the well-known Le Chatelier's principle (Le Chatelier and Boudouard, 1898). A value of 0.5 bar Ar in the tube before sealing provided a reasonable balancing between the material purity and the stability of the ampule against the internal gas pressure, increasing with the temperature.

The obtained samples represented well-crystallized and homogeneous dark-gray or brownish powders. Typical experimental powder X-ray diffractograms of $Li_2Fe_{0.9}M_{0.1}SO$ are shown in **Figure 1** together with their cell parameters calculated from Rietveld refinement.

As one would expect from the values of ionic radii for transition metal cations (Shannon, 1976), partial substitution of high-spin HS–Fe^{2+} (0.78 Å) by HS–Co^{2+} (0.745 Å) must result in a slight shrinkage of the crystallographic unit cell, whereas HS–Mn^{2+} (0.83 Å) enhances the cell parameter. The values of cell metrics for $Li_2Fe_{0.9}Mn_{0.1}SO$ and pure Li_2FeSO obtained in this work agree well with the results of the previous research related to these materials (Mikhailova et al., 2018; Gorbunov et al., 2020). For the Co-containing phase as expected, the determined cell parameter of 3.9082(5) Å is slightly smaller than that of unsubstituted Li_2FeSO material (3.914 Å).

Transmission electron microscopy-micrographs of the $Li_2Fe_{0.9}Co_{0.1}SO$ material are given in the **Supplementary Material** (**Supplementary Figures 1, 2**). From these pictures, one can see the polycrystalline nature of the material and homogeneous distribution of the elements.

Electrochemical Investigations of $Li_2Fe_{0.9}M_{0.1}SO$ Materials

At first, cyclic voltammetry and rate capability measurements of substituted materials and the Li_2FeSO reference were carried out, see **Figures 2A–D**. Cyclic voltammograms show that these three materials undergo a similar and complex mechanism of lithium extraction during the first cycle. Three oxidative peaks are observed for all materials (**Figures 2A–C**), while during reduction, two redox peaks are present down to 1.5 V vs. Li in the case of Li_2FeSO and $Li_2Fe_{0.9}Co_{0.1}SO$, and an additional peak around 1.55 V is seen for $Li_2Fe_{0.9}Mn_{0.1}SO$. The reduction peak between 2.0 and 2.4 V in all materials represents most probably a combination of two peaks, which are not well-resolved. During the second and the third cycles, the fourth peak appears on each of the oxidation curves, and all peaks are becoming less resolved. The form of the reduction curve changes more in the case of Co- and Mn-substituted materials in comparison to Li_2FeSO. Thus, the reduction peak around 1.55 V disappears almost entirely in $Li_2Fe_{0.9}Mn_{0.1}SO$, while the peak around 2.23 V is shifted to 2.10 V for $Li_2Fe_{0.9}Co_{0.1}SO$. As the differences in maxima positions of oxidation and redox peaks for all materials are significantly higher than the $2.3 \times \frac{RT}{nF} \approx 0.059$ V empirical criterium (Bard and Faulkner, 1980), it is very probable that materials suffer from serious kinetic obstacles during the discharge process. This observation is further quantitatively proved in the section with GITT measurements.

The results of rate capability tests demonstrate that insertion of even a small amount of manganese into the crystal lattice influences negatively the performance of the material in the Li-battery, especially at high current densities, whereas partial substitution of iron by cobalt provides a significant improvement of the electrochemical properties.

As $Li_2Fe_{0.9}Co_{0.1}SO$ shows higher specific capacity values and $Li_2Fe_{0.9}Mn_{0.1}SO$ much lower capacities at different current densities in comparison to the Li_2FeSO reference, only $Li_2Fe_{0.9}Co_{0.1}SO$ and Li_2FeSO were further subjected to

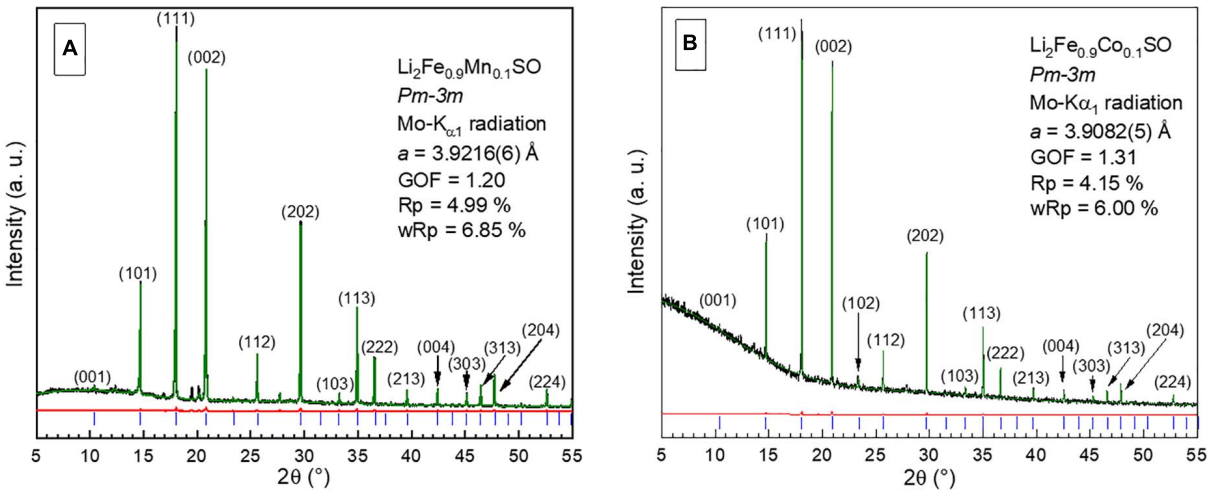

FIGURE 1 | Typical experimental diffractograms (black) of **(A)** $Li_2Fe_{0.9}Mn_{0.1}SO$ and **(B)** $Li_2Fe_{0.9}Co_{0.1}SO$ materials, together with the calculated (green) and difference (red) curves. Bragg positions are shown by blue dashes. Unindexed peaks in part **(A)** correspond to a small amount of metal sulfides.

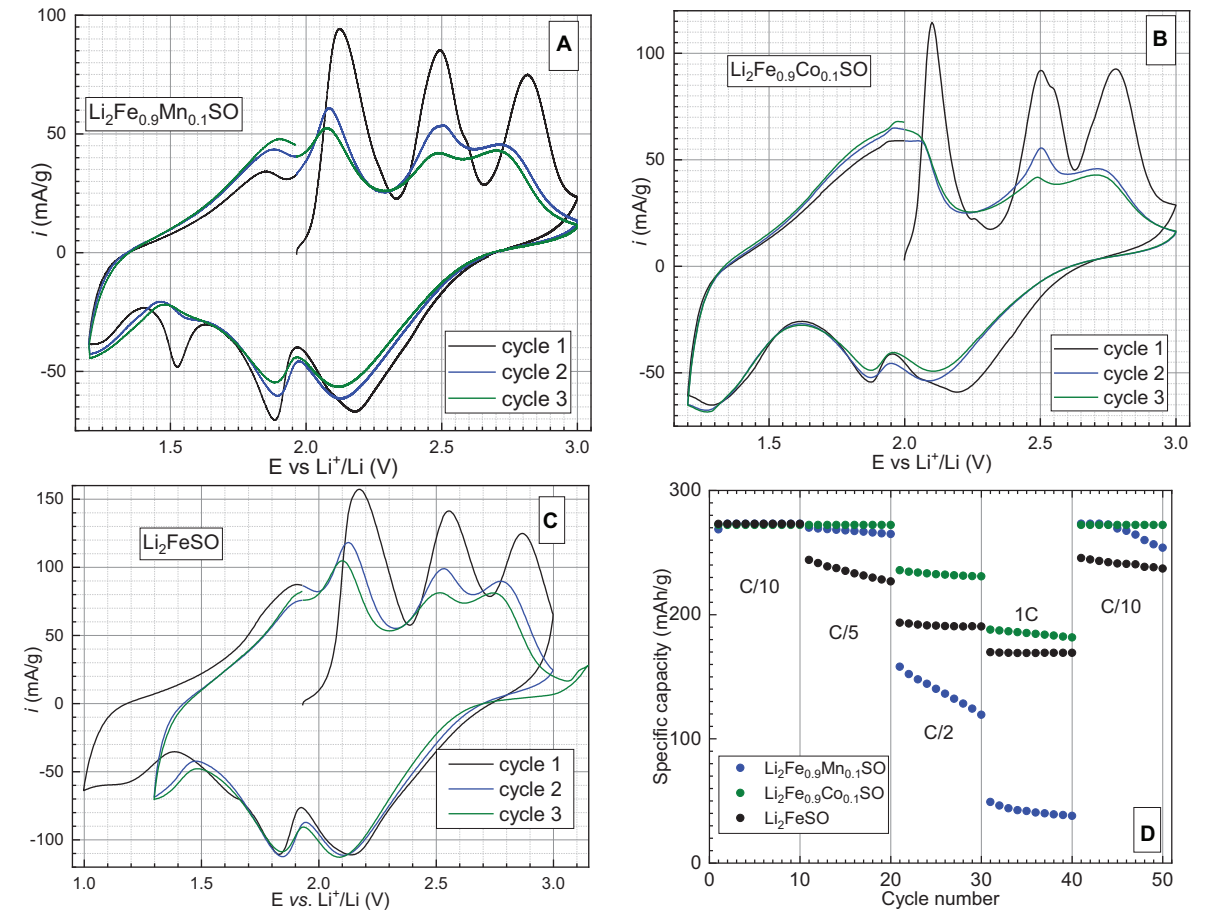

FIGURE 2 | Low scan rate cyclic voltammograms of **(A)** $Li_2Fe_{0.9}Mn_{0.1}SO$. **(B)** $Li_2Fe_{0.9}Co_{0.1}SO$ and **(C)** Li_2FeSO reference material recorded at 0.05 mV/s sweeping rate. **(D)** Specific discharge capacities of $Li_2Fe_{0.9}M_{0.1}SO$ (M–Co, Mn) and Li_2FeSO materials at different current rates. Rate capability tests were performed two times for each material. The selected charge-discharge curves for Co-containing material which performed the best, are available in the **Supplementary Material** (**Supplementary Figure 3**).

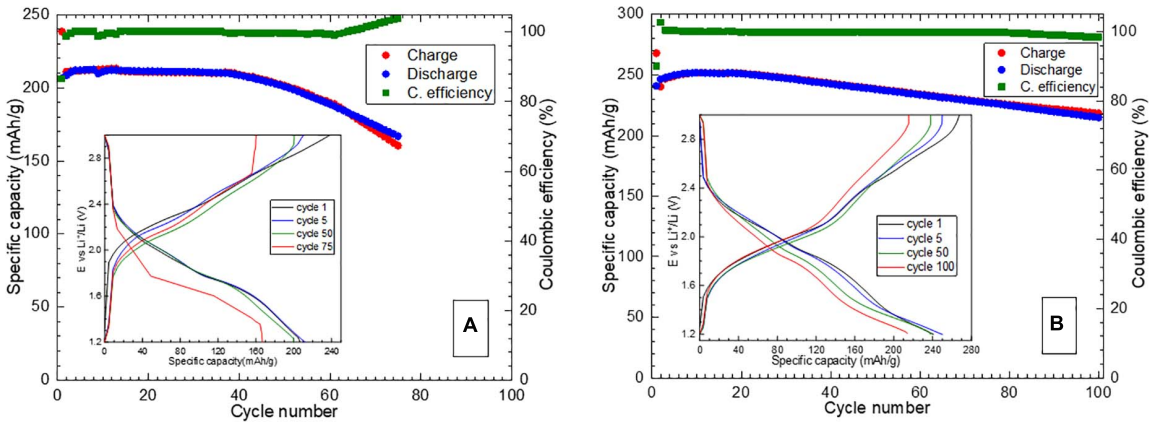

FIGURE 3 | Specific capacity and Coulombic efficiency results of long-term cycling of **(A)** Li_2FeSO and **(B)** $Li_2Fe_{0.9}Co_{0.1}SO$ at 1C current density. Insets–selected galvanostatic charge/discharge curves.

long-term cycling at 1C current density. The results are presented in **Figure 3**.

As one can see from the corresponding figures, partial substitution of 10% Fe by 10% Co in the Li_2FeSO antiperovskite structure results in a better electrochemical performance in terms of specific capacity, Coulombic efficiency and capacity retention when cycled at 1C current density.

Although it suffered from a significant capacity loss, the $Li_2Fe_{0.9}Co_{0.1}SO$ material delivered more than 80% of the initial specific capacity value at 1C even after 100 cycles. The unsubstituted Li_2FeSO material reached 80% of the initial capacity at 75th cycle already, thus showing the advantage of the Co-containing phase as a battery material. The initial values of Coulombic efficiency were around 100% for both materials and decayed slightly after 100 cycles for $Li_2Fe_{0.9}Co_{0.1}SO$, whereas for Li_2FeSO, after 60th cycle a discharge capacity became higher than a charge one.

The results of galvanostatic intermittent titration experiments for the first charge and discharge processes are presented in **Supplementary Figure 4**. It was observed that partial substitution of iron by other transition metals in the cubic antiperovskite structure generally results in a slight decay of the average Li-diffusion coefficient during the charge. Moreover, the rapid deterioration of the diffusion process at the end of the charge, corresponding to a significant decrease of the diffusion coefficient, occurs earlier for the substituted materials (2.7 V vs. 2.88 V for Li_2FeSO). However, the effect of partial substitution is opposite for the discharge process: the average Li-diffusion coefficient for substituted phases is one order of magnitude higher than for Li_2FeSO (Mikhailova et al., 2018). No direct correlation between the lattice parameter *a* and the lithium diffusion coefficient was observed. The iron to cobalt substitution results in a slight shrinkage of the unit cell which is opposite to the effect of iron to manganese substitution. Nevertheless, both additional cations improved the kinetics of the discharge process at least during the first cycle by a comparable value. Note, despite a noticeably higher values for the diffusion coefficient during the discharge process compared to unsubstituted Li_2FeSO, the $Li_2Fe_{0.9}Mn_{0.1}SO$ material performs worse in terms of rate capability.

Operando XRD Studies

In order to evaluate structural changes in $Li_2Fe_{0.9}Mn_{0.1}SO$ and $Li_2Fe_{0.9}Co_{0.1}SO$ during Li-removal and insertion, *operando* XRD studies were carried out, with the results presented in **Figures 6**, **7**, respectively. Corresponding galvanostatic charge-discharge curves are shown in the **Supplementary Material** (**Supplementary Figure 5**).

The $Li_2Fe_{0.9}Mn_{0.1}SO$ material demonstrates a structural behavior with the formation of a second phase (**Figure 4**), similar to the one reported earlier for $Li_2Fe_{0.5}Mn_{0.5}SO$ (Gorbunov et al., 2020). The relative change of the lattice parameter for both Mn-substituted materials during the completed charge is around 0.8%. Both of them exhibit a two-phase delithiation mechanism with an accumulation of the second isostructural phase with a lower cell parameter during each subsequent cycle. The first difference between these two materials includes the amount of lithium extracted from the structure before the second phase appears. In the case of $Li_2Fe_{0.5}Mn_{0.5}SO$, the amount of remaining structural lithium was around 1.7. In case of $Li_2Fe_{0.9}Mn_{0.1}SO$, the second phase appears earlier, when the amount of lithium in the structure is equal to 1.8. The second difference is that in contrast to $Li_2Fe_{0.5}Mn_{0.5}SO$, the phase with the higher cell parameter does not completely transform to the phase with the low cell parameter during delithiation at the first two cycles, even when a large amount of lithium is extracted from the structure of $Li_2Fe_{0.9}Mn_{0.1}SO$.

The structural behavior of the $Li_2Fe_{0.9}Co_{0.1}SO$ material (**Figure 5**) strongly resembles that of Li_2FeSO. No formation of a second isostructural phase was observed, and the change of the lattice parameter is highly non-linear during the charging process, similar to the reported behavior for Li_2FeSO (Mikhailova et al., 2018). The amount of extracted lithium before this non-linearity appears, is different, though. For Li_2FeSO, the extracted Li-amount corresponding to the first minimum in the lattice parameter *a* is around 0.4, while for $Li_2Fe_{0.9}Co_{0.1}SO$ it is almost

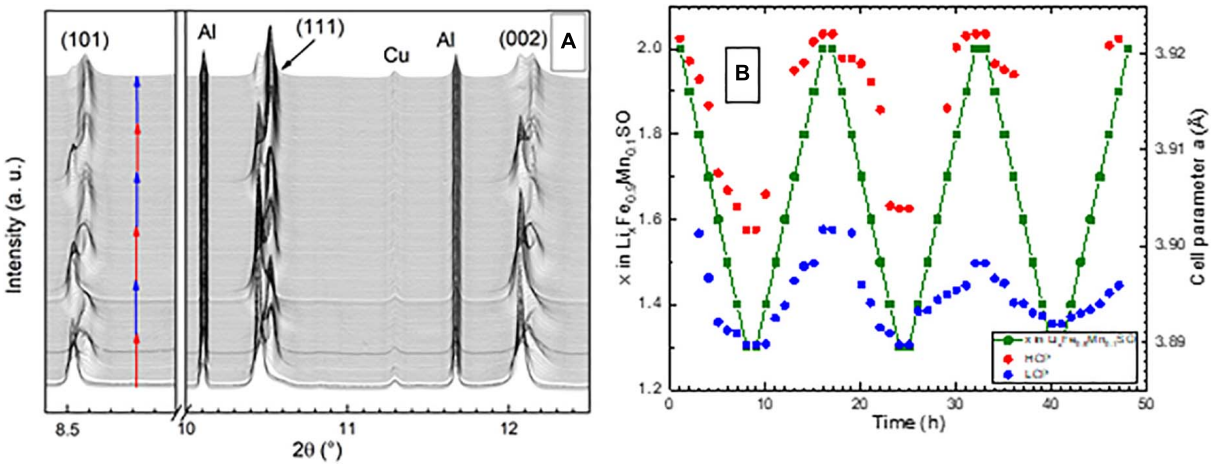

FIGURE 4 | (A) Part of X-ray diffractograms taken *operando* on ALBA (Barcelona). Red arrows show charge and blue–discharge process. The wavelength was 0.41240 Å. **(B)** Cell parameter of $Li_2Fe_{0.9}Mn_{0.1}SO$ versus time, and the amount of lithium in the structure during *operando* XRD measurements. HCP and LCP mean "phase with high cell parameter value" and "phase with low cell parameter value", respectively.

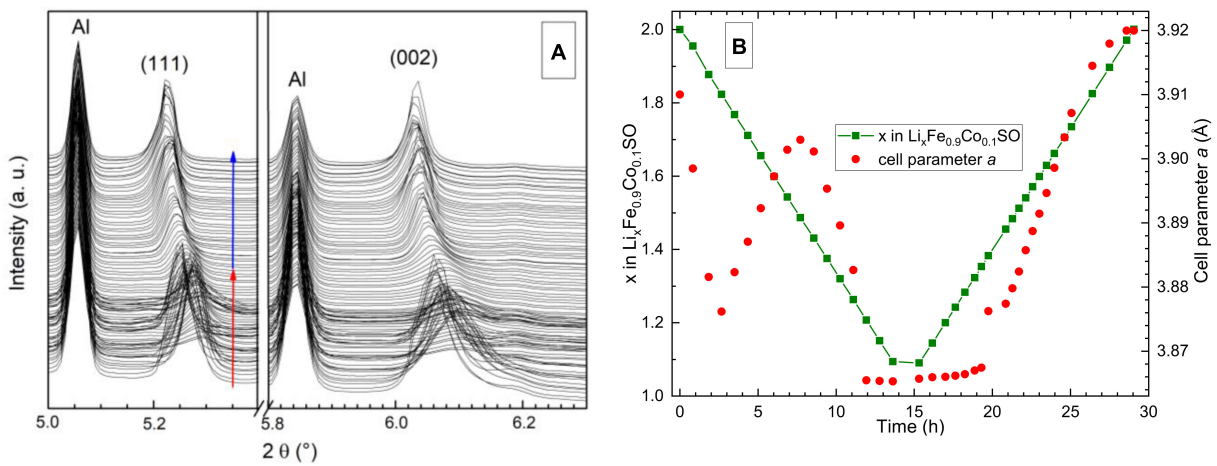

FIGURE 5 | (A) Part of X-ray diffractograms taken *operando* on DESY (Hamburg). Red arrows show charge and blue–discharge process. The wavelength was 0.20741 Å. **(B)** Cell parameter of $Li_2Fe_{0.9}Co_{0.1}SO$ versus time, and the amount of lithium in the structure during *operando* XRD measurements.

equal to 0.2. We should mention here that the Co-substituted phase remains crystalline during the whole charge-discharge cycle, in contrast to Li_2FeSO, thus allowing structural analysis during the complete (de)lithiation process.

As visible from drastically decreased intensities of Bragg reflections combined with their broadening on *operando* X-ray diffractograms, both $Li_2Fe_{0.9}Mn_{0.1}SO$, and $Li_2Fe_{0.9}Co_{0.1}SO$ suffer from a severe degree of structural strains while being charged. However, their crystal symmetry remains constant all the time, and the microstructural effects are regained almost completely after the first cycle.

Operando XAS Studies

Analysis of the *operando* recorded X-ray absorption spectra provided information about redox activities of Fe^{2+} and M^{2+} cations during cycling and allowed to disclose the local environment of the scattering atoms (Newville, 2004) while lithium was reversibly extracted from the lattice.

The results of *operando* XAS studies of $Li_2Fe_{0.9}Co_{0.1}SO$ and $Li_2Fe_{0.9}Mn_{0.1}SO$ are presented in **Figures 6**, **7**, respectively. The corresponding galvanostatic charge-discharge curves are available in the **Supplementary Material** (**Supplementary Figure 6**). For both materials, two tendencies were observed. Firstly, both Co and Mn are electrochemically active. Secondly, the average oxidation state of iron in materials with Co and Mn, calculated with involving the Fe^{2+} and Fe^{3+} references, changes from +2 to +2.9, and the process is almost reversible (see **Supplementary Figure 7**). $Li_2Fe_{0.9}Mn_{0.1}SO$, similar to $Li_2Fe_{0.5}Mn_{0.5}SO$ with a much higher Mn-substitution grade (Gorbunov et al., 2020), shows a low redox activity of manganese: even when 1.1 Li^+ per formula unit are extracted from $Li_2Fe_{0.9}Mn_{0.1}SO$, the average oxidation state of Mn does

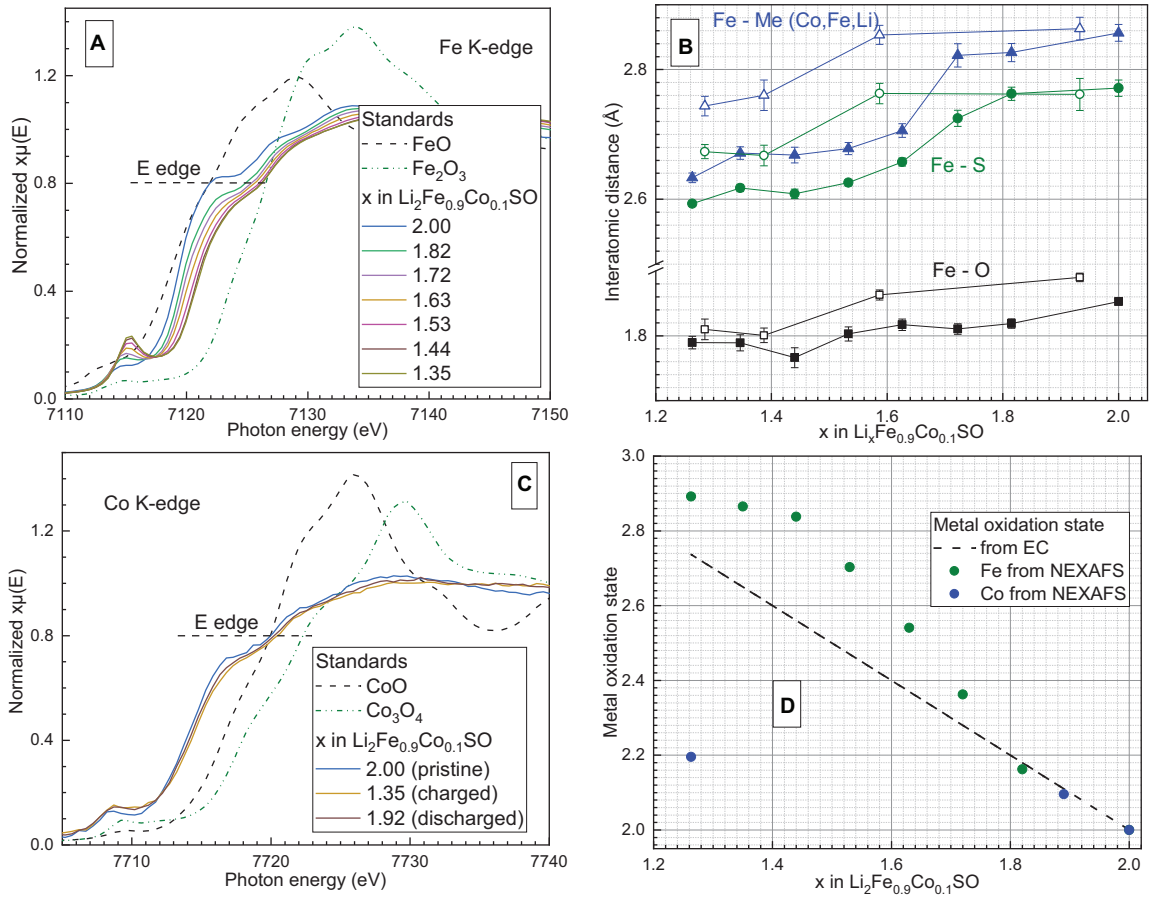

FIGURE 6 | (A) Normalized Fe K-edge X-ray absorption spectra of $Li_2Fe_{0.9}Co_{0.1}SO$ recorded *operando*. **(B)** Average interatomic distances between iron and other atoms estimated by extended X-ray absorption fine structure analysis with their confidence intervals. Filled points correspond to the charging process, unfilled–to the discharging. The scale of the Y-axis is the same before and after the break. **(C)** Normalized Co K-edge X-ray absorption spectra of the same material recorded *operando*. **(D)** Average oxidation states of metal cations in $Li_2Fe_{0.9}Co_{0.1}SO$ estimated from the electrochemical measurements (EC) and XAS studies. The position of the Fe K-edge was defined as the energy at the X-ray absorption coefficient $\mu(E)$ = 0.8 of normalized post-edge intensities, similar to Mikhailova et al. (2018) and Gorbunov et al. (2020).

not exceed the value of around +2.2. In contrast, cobalt in $Li_2Fe_{0.9}Co_{0.1}SO$ exhibits a noticeably higher redox activity, having nearly the same average value of +2.2 when only 0.65 Li per formula unit is extracted.

Next, we performed an extended X-ray absorption fine structure analysis, which provided local structural information about the first and second coordination spheres of Fe ions in the $Li_2Fe_{0.9}Co_{0.1}SO$ and $Li_2Fe_{0.9}Mn_{0.1}SO$ materials. An example of the EXAFS fit is given in the **Supplementary Material** (**Supplementary Figure 8**). Note, since the cation site in the antiperovskite structure is randomly occupied by lithium, iron and cobalt or manganese, diffraction methods provide information about the average local surrounding for this cation site. In opposite, EXAFS analysis of the Fe K-edge spectra allows us to separately evaluate the local structure of Fe cations.

Comparison of interatomic distances calculated from EXAFS and synchrotron XRD shows that for both substituted antiperovskites, the XRD analysis provides significantly longer metal-oxygen distances and shorter metal-metal distances than the EXAFS analysis, see **Table 1**. This difference points to the distortion of the local structural surrounding for Fe-cations comparing to the average structure. For example, the Fe–O bond length of 1.85 Å in $Li_2Fe_{0.9}Co_{0.1}SO$ is well below the average (Fe, Li, Co)–O distance of 1.955 Å. Moreover, a smaller difference between individual Fe–O and average (Fe, Li, metal)–O distances in $Li_2Fe_{0.9}Mn_{0.1}SO$ comparing to $Li_2Fe_{0.9}Co_{0.1}SO$ argues for a higher stabilizing effect of Mn^{2+} cations in comparison to Co^{2+} in the initial composition before delithiation.

Next, due to the symmetry reason, metal–sulfur and metal–metal distances should be equal to each other in the averaged crystal structure, giving 2.765 Å in $Li_2Fe_{0.9}Co_{0.1}SO$ and 2.773 Å in $Li_2Fe_{0.9}Mn_{0.1}SO$, according to the XRD measurements. However, the EXAFS calculations show a significant discrepancy between Fe–metal and Fe–S distances. For example, the Fe–metal and Fe–S distances in $Li_2Fe_{0.9}Co_{0.1}SO$ were calculated as 2.86 and 2.77 Å, respectively. The $Li_2Fe_{0.9}Mn_{0.1}SO$ material provides a similar issue having the Fe-metal distance of 2.91 Å and the Fe–S distance of 2.75 Å. Therefore, the antiperovskite structure

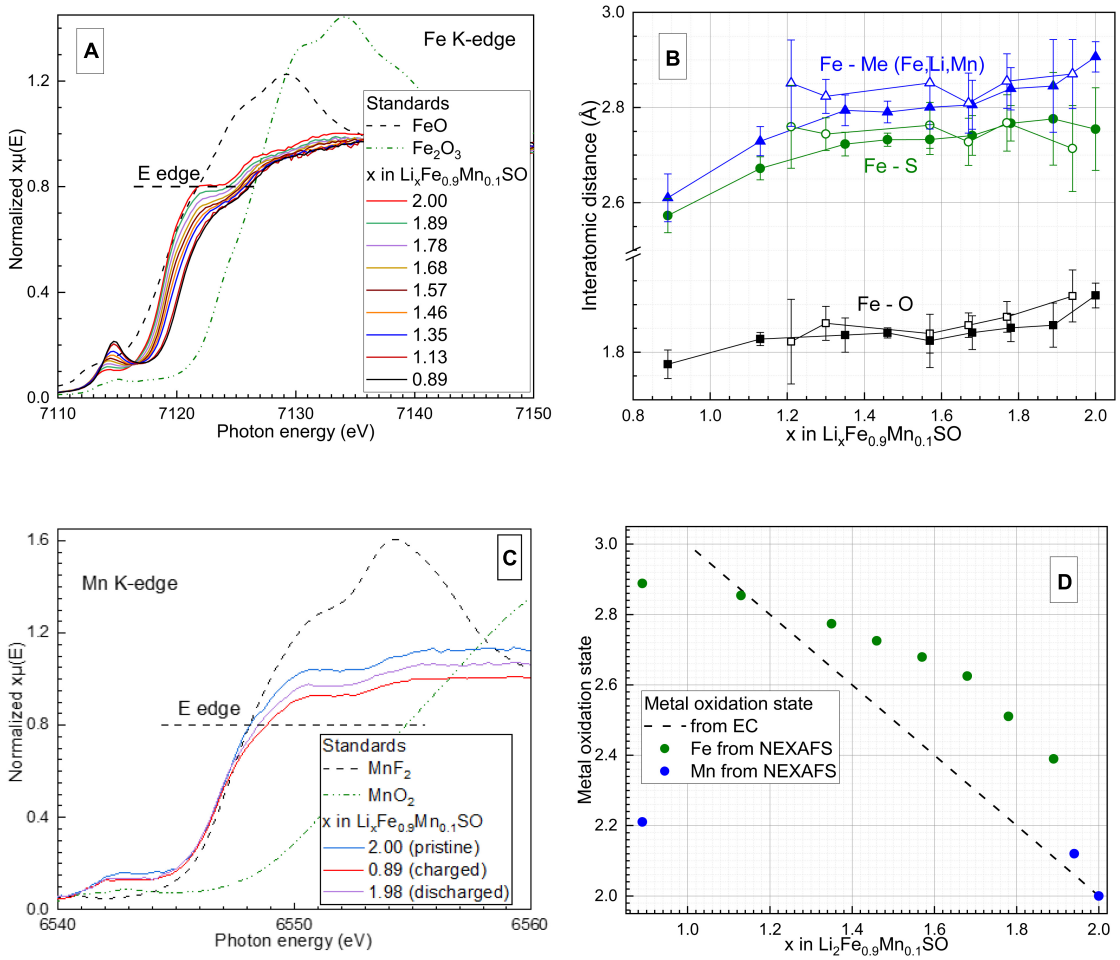

FIGURE 7 | (A) Normalized Fe K-edge X-ray absorption spectra of $Li_2Fe_{0.9}Mn_{0.1}SO$ recorded *operando*. **(B)** Average interatomic distances for iron estimated by extended X-ray absorption fine structure calculations with their confidence intervals. Filled points correspond to the charging, unfilled–to the discharging process. The scale of the Y-axis is the same before and after the break). **(C)** Normalized Mn K-edge X-ray absorption spectra of the same material recorded *operando*. **(D)** Average oxidation states of metals in $Li_2Fe_{0.9}Mn_{0.1}SO$ estimated from the electrochemical measurements and XAS studies. The position of the Fe K-edge was defined as the energy at the X-ray absorption coefficient $\mu(E) = 0.8$ of normalized post-edge intensities as well.

TABLE 1 | Interatomic distances in pristine $Li_2Fe_{0.9}Co_{0.1}SO$ and $Li_2Fe_{0.9}Mn_{0.1}SO$ materials calculated from synchrotron XRD and EXAFS data analysis.

Compound	XRD		EXAFS	
	Atoms	Interatomic distance (Å)	Atoms	Interatomic distance (Å)
$Li_2Fe_{0.9}Co_{0.1}SO$	(Fe, Li, Co)–O	1.955 (1)	Fe–O	1.85 (1)
	(Fe, Li, Co)–(Fe, Li, Co)	2.765 (1)	Fe–(Fe, Li, Co)	2.86 (1)
	(Fe, Li, Co)–S	2.765 (1)	Fe–S	2.77 (1)
$Li_2Fe_{0.9}Mn_{0.1}SO$	(Fe, Li, Mn)–O	1.961 (6)	Fe–O	1.92 (2)
	(Fe, Li, Mn)–(Fe, Li, Mn)	2.773 (6)	Fe–(Fe, Li, Mn)	2.91 (3)
	(Fe, Li, Mn)–S	2.773 (6)	Fe–S	2.75 (9)

is probably stabilized by Fe–S bonds, as their lengths are very close to the average value from XRD, while Fe–O bonds bring instability through a substantial deviation from the average value.

Note, the longer Fe–metal distance in comparison to the Fe–S one was also observed for the Li_2FeSO material (Mikhailova et al., 2018). However, in Li_2FeSO, the difference is much smaller, never exceeding the value of around 0.01 Å, and only appearing when around 0.2 Li is extracted.

During delithiation, all interatomic distances decrease for $Li_2Fe_{0.9}Co_{0.1}SO$ and $Li_2Fe_{0.9}Mn_{0.1}SO$, thus confirming metal oxidations (**Figures 6B**, **7B**). Interestingly, for both materials the Fe–S bond length decreases stronger than the Fe–O

length, thus reflecting higher compressibility of S^{2-} anion in comparison to O^{2-}.

DISCUSSION

$Li_2Fe_{1-x}M_xSO$ antiperovskites represent a class of cathode materials with electrochemical performance and redox reaction mechanism during delithiation strongly dependent on the nature and the amount of M cation. Previously, we showed that replacement of a half Fe^{2+} cations in the structure by Mn^{2+} generally leads to deterioration of the electrochemical properties in terms of the specific capacity, cycling stability and rate capability (Gorbunov et al., 2020). One possible reason for this may be an impeded kinetics of Mn^{2+} to Mn^{3+} oxidation during Li-removal since it was clearly shown that at first, a significant part of Fe^{2+} cations was oxidized, and only afterwards Mn^{2+} started to participate in the redox process. However, the structural changes in $Li_2Fe_{0.5}Mn_{0.5}SO$ during Li-extraction were quite different in comparison to Li_2FeSO: (i) the crystallinity of the substituted material was preserved without any structure collapse during whole charge and discharge, (ii) no new Bragg reflections of unknown origin at small 2θ values appeared in diffraction patterns of $Li_2Fe_{0.5}Mn_{0.5}SO$ during battery charge, (iii) a second isostructural phase with a smaller lattice parameter *a* formed, remaining as a single phase at the end of delithiation, and (iv) a nearly linear decrease of the lattice parameter *a* was observed with decreased Li-content upon entire delithiation/lithiation process (Gorbunov et al., 2020).

From the present study, it is evidenced that even a small degree of Fe-substitution in Li_2FeSO by other metal cations can also lead to significant property changes in dependence on the metal. In this sense, the roles of Mn^{2+} and Co^{2+} ions in the structure are quite different for electrochemical characteristics. The introduction of 10% Co^{2+} into the Li_2FeSO structure results in a noticeable improvement of the electrochemical performance in comparison to Li_2FeSO, whereas the presence of 10% Mn^{2+} drastically worsens it. Interestingly, a slow charge and discharge of batteries with these three materials provides very similar specific capacity values for the first several cycles (**Figure 2D**). Essential differences between the materials arise after cycling at higher current densities, thus reflecting kinetical obstacles for the materials with different compositions. A couple of facts may be the reason for this finding.

Thereby, the replacement of 10% of Fe via Mn or Co in Li_2FeSO stabilizes the crystal structure of the antiperovskite during delithiation, leading to the maintenance of crystallinity at least for the several first cycles. Nevertheless, partially or almost amorphous Li_2FeSO performs better at high current densities than the crystalline $Li_2Fe_{0.9}Mn_{0.1}SO$ material, demonstrating a two-phase mechanism of lithium extraction and insertion. Therefore, Li-diffusion is more suppressed through the formations of the second isostructural phase than through the amorphization process. The reason for the building of the second phase in the $Li_2Fe_{0.9}Mn_{0.1}SO$ material relies most probably on Jahn-Teller effect (Bunker and Jensen, 1998) known for Mn^{3+} cations, which form during delithiation. Since the ionic radius of high-spin Mn^{2+} (0.83 Å) is much larger than the radius of high-spin Mn^{3+} (0.645 Å) or low-spin Mn^{3+} (0.58 Å), the oxidation of Mn^{2+} results in the appearance of the second phase with a smaller lattice parameter *a*. As the Mn^{3+}/Mn^{2+} redox process is not entirely reversible in $Li_2Fe_{0.9}Mn_{0.1}SO$, the strains may accumulate in the bulk material with the time, thus impeding the migration of lithium ions. Moreover, this phase transformation must result in reducing the particle size and even nano-structuring of the material with time, as it was observed previously for the $Li_2Fe_{0.5}Mn_{0.5}SO$ material (Gorbunov et al., 2020).

In this sense, cobalt in $Li_2Fe_{0.9}Co_{0.1}SO$ seems to serve as a structure stabilizer during Li-removal. A difference between ionic radii for high-spin Co^{2+} (0.745 Å) and high-spin Co^{3+} (0.61 Å) or low-spin Co^{3+} (0.545 Å) is less pronounced than in the case of Mn cations. If the same amount of lithium is extracted, $Li_2Fe_{0.9}Co_{0.1}SO$ shows the lowest relative change of the lattice parameter *a* comparing to $Li_2Fe_{0.9}Mn_{0.1}SO$ and Li_2FeSO, which may be a reason for the fact that this material outperforms the other two compositions studied here. On the other hand, the entire replacement of Fe by Co to the Li_2CoSO compound leads to significant decrease of the specific capacity down to 70 mAh/g as it was found in work (Lai et al., 2018).

No direct correlation was observed between the lattice parameters of Li_2FeSO, $Li_2Fe_{0.9}Co_{0.1}SO$, and $Li_2Fe_{0.9}Mn_{0.1}SO$, and the values of Li^+ diffusion coefficient, either on charge or discharge. However, it should be noted that the Li-diffusion coefficient was determined for the materials at the first cycle only.

Despite a significant improvement of electrochemical performance by introducing a small amount of cobalt into the crystal structure of Li_2FeSO, the origin of the capacity loss of *Pm-3m* antiperovskites still needs to be clarified. The average operation voltage and the form of the discharge profile may be improved as well. Further studies are needed for exploring the chemical flexibility of antiperovskites and resulting electrochemical characteristics. For example, partial Fe-substitution in the Li_2FeSO material by a redox-inactive cation, serving only as a structure stabilizer would be an exciting point and is already the topic for future work. In order to overcome kinetics issues and to enhance cyclic stability of antiperovskite materials, various morphology modifications may be useful (Yi et al., 2020a,b). This would be a further step to improve the materials in terms of battery application.

DATA AVAILABILITY STATEMENT

The raw data supporting the conclusions of this article will be made available by the authors, without undue reservation.

AUTHOR CONTRIBUTIONS

MG and DM are the corresponding authors. SC, IG, and VB contributed to the manuscript preparation equally. All authors contributed to the article and approved the submitted version.

FUNDING

This work was supported by the European Regional Development Fund through *Sächsische Aufbaubank* and project LUKSIAK (Project number 100350438). MG and SC thank the IFW excellence program for the financial support.

ACKNOWLEDGMENTS

The authors acknowledge to Martin Valldor (Department of Chemistry, University of Oslo, Norway) for the discussion regarding materials synthesis. This research has benefitted from beamtime allocation at beamlines P02.1 and P65 at the PETRA III synchrotron (DESY, Hamburg, Germany), and BL04 at the ALBA Cells synchrotron (Barcelona, Spain).

SUPPLEMENTARY MATERIAL

The Supplementary Material for this article can be found online at: https://www.frontiersin.org/articles/10.3389/fenrg.2021.657962/full#supplementary-material

Supporting Information | Supporting Information includes results of TEM characterization of $Li_2Fe_{0.9}Co_{0.1}SO$, galvanostatic charge-discharge curves recorded during *operando* XRD and XAS measurements, Fe K-edge spectra of $Li_2Fe_{0.9}Co_{0.1}SO$ and $Li_2Fe_{0.9}Mn_{0.1}SO$ materials at almost charged and discharged states, and an example of EXAFS fit together with some structural information.

REFERENCES

Bard, A. J., and Faulkner, L. R. (1980). *Electrochemical Methods: Fundamentals and Applications*. New York, NY: Wiley.

Bukun, N. G., Domashnev, I. A., Moskvina, E. I., and Ukshe, E. A. (1998). Synthesis and electric conductivity of a NASICON-type solid electrolyte. *Neorg. Mater. Inorg. Mater.* 24, 360–364.

Bunker, P. R., and Jensen, P. (1998). *Molecular Symmetry and Spectroscopy*, 2nd Edn. Ottawa, ON: NRC Research Press.

Demourgues Guerlou, L., Braconnier, J. J., and Delmas, C. (1993). Iron-substituted nickel oxyhydroxides and hydroxides obtained by chimie douce. *J. Solid State Chem.* 104, 359–367. doi: 10.1006/jssc.1993.1171

Dippel, A. C., Liermann, H. P., Delitz, J. T., Walter, P., Schulte-Schrepping, H., Seeck, O. H., et al. (2015). Beamline P02.1 at PETRA III for high-resolution and high-energy powder diffraction. *J. Synchrotron Radiat.* 22, 675–687. doi: 10.1107/s1600577515002222

Fauth, F., Peral, I., Popescu, C., and Knapp, M. (2013). The new material science powder diffraction beamline at ALBA synchrotron. *Powder Diffr.* 28, 360–370.

Gorbunov, M. V., Carrocci, S., Maletti, S., Valldor, M., Doert, T., Hampel, S., et al. (2020). Synthesis of $(Li_2Fe_{1-y}Mn_y)SO$ antiperovskites with comprehensive investigations of $(Li_2Fe_{0.5}Mn_{0.5})SO$ as cathode in Li-ion batteries. *Inorg. Chem.* 59, 15626–15635. doi: 10.1021/acs.inorgchem.0c01753

Herklotz, M., Weiß, J., Ahrens, E., Yavuz, M., Mereacre, L., Kiziltas-Yavuz, N., et al. (2016). A novel high-throughput setup for in situ powder diffraction on coin cell batteries. *J. Appl. Crystallogr.* 49, 340–345. doi: 10.1107/s1600576715022165

Lai, K. T., Antonyshyn, I., Prots, Y., and Valldor, M. (2017). Anti-perovskite li-battery cathode materials. *J. Am. Chem. Soc.* 28, 9645–9649. doi: 10.1021/jacs.7b04444

Lai, K. T., Antonyshyn, I., Prots, Y., and Valldor, M. (2018). Extended chemical flexibility of cubic anti-perovskite lithium battery cathode materials. *Inorg. Chem.* 57, 13296–13299. doi: 10.1021/acs.inorgchem.8b01850

Le Chatelier, H., and Boudouard, O. (1898). Limits of flammability of gaseous mixtures. *Bull. Soc. Chim. Fr.* 19, 483–488.

Lu, Z., and Ciucci, F. (2018). Anti-perovskite cathodes for lithium batteries. *J. Mater. Chem. A* 6, 5185–5192. doi: 10.1039/c7ta11074j

Mikhailova, D., Giebeler, L., Maletti, S., Oswald, S., Sarapulova, A., Indris, S., et al. (2018). Operando studies of antiperovskite lithium battery cathode material $(Li_2Fe)SO$. *ACS Appl. Energy Mat.* 1, 6593–6599. doi: 10.1021/acsaem.8b01493

Newville, M. (2004). *Fundamentals of XAFS, Revision 1.7*. Chicago, IL: University of Chicago.

Padhi, A. K., Nanjundaswamy, K. S., Masquelier, C., Okada, S., and Goodenough, J. B. (1997). Effect of structure on the Fe^{3+}/Fe^{2+} redox couple in iron phosphates. *J. Electrochem. Soc.* 144, 1609–1613.

Petricek, V., Dusek, M., and Palatinus, L. (2014). Crystallographic computing system JANA2006: general features. *Z. Kristallogr. Crystallogr. Mater.* 229, 345–352.

Ravel, B., and Newville, M. (2005). ATHENA, ARTEMIS, HEPHAESTUS: data analysis for X-ray absorption spectroscopy using IFEFFIT. *J. Synchrotron Radiat.* 12, 537–541. doi: 10.1107/s0909049505012719

Rietveld, H. M. (1969). A profile refinement method for nuclear and magnetic structures. *J. Appl. Crystallogr.* 2, 65–71. doi: 10.1107/s0021889869006558

Shannon, R. D. (1976). Revised effective ionic radii and systematic studies of interatomic distances in halides and chalcogenides. *Acta Crystallogr.* 32, 751–767. doi: 10.1107/s0567739476001551

Thackeray, M. M., David, W. I. F., Bruce, P. G., and Goodenough, J. B. (1983). Lithium insertion into manganese spinels. *Mater. Res. Bull.* 18, 461–472. doi: 10.1016/0025-5408(83)90138-1

Welter, E., Chernikov, R., Herrmann, M., and Nemausat, R. (2018). A beamline for bulk sample x-ray absorption spectroscopy at the high brilliance storage ring PETRA III. *AIP Conf. Proc.* 2054:040002.

Weppner, W., and Huggins, R. A. (1977). Determination of the kinetic parameters of mixed-conducting electrodes and application to the system Li_3Sb. *J. Electrochem. Soc.* 124, 1569–1578. doi: 10.1149/1.2133112

Wu, F., Maier, J., and Yu, Y. (2020). Guidelines and trends for next-generation rechargeable lithium and lithium-ion batteries. *Chem. Soc. Rev.* 49, 1569–1614. doi: 10.1039/c7cs00863e

Yi, T.-F., Pan, J.-J., Wei, T.-T., Li, Y., and Cao, G. (2020a). $NiCo_2S_4$-based nanocomposites for energy storage in supercapacitors and batteries. *Nano Today* 33:100894. doi: 10.1016/j.nantod.2020.100894

Yi, T.-F., Wei, T.-T., Li, Y., He, Y.-B., and Wang, Z.-B. (2020b). Efforts on enhancing the Li-ion diffusion coefficient and electronic conductivity of titanate-based anode materials for advanced Li-ion batteries. *Energy Storage Mater.* 26, 165–197. doi: 10.1016/j.ensm.2019.12.042

Conflict of Interest: The authors declare that the research was conducted in the absence of any commercial or financial relationships that could be construed as a potential conflict of interest.